



Feasibility of solid oxide fuel cell dynamic hydrogen coproduction to meet building demand



Brendan Shaffer, Jacob Brouwer*

National Fuel Cell Research Center, University of California, Irvine, CA 92697-3550, USA

HIGHLIGHTS

- A dynamic internal reforming-solid oxide fuel cell system model is developed.
- Electricity and hydrogen coproduction to meet dynamic building demand is modeled.
- The co-producing system well follows the measured building electric load dynamics.
- Dynamic operation of an SOFC system for co-producing hydrogen is demonstrated.
- Thermal and tank filling responses to dynamic operation are presented.

ARTICLE INFO

Article history:

Received 2 February 2013

Received in revised form

5 August 2013

Accepted 29 August 2013

Available online 18 September 2013

Keywords:

Hydrogen

Coproduction

SOFC

Internal reformation

Buildings

Dynamic

ABSTRACT

A dynamic internal reforming-solid oxide fuel cell system model is developed and used to simulate the coproduction of electricity and hydrogen while meeting the measured dynamic load of a typical southern California commercial building. The simulated direct internal reforming-solid oxide fuel cell (DIR-SOFC) system is controlled to become an electrical load following device that well follows the measured building load data (3-s resolution). The feasibility of the DIR-SOFC system to meet the dynamic building demand while co-producing hydrogen is demonstrated. The resulting thermal responses of the system to the electrical load dynamics as well as those dynamics associated with the filling of a hydrogen collection tank are investigated. The DIR-SOFC system model also allows for resolution of the fuel cell species and temperature distributions during these dynamics since thermal gradients are a concern for DIR-SOFC.

© 2013 Elsevier B.V. All rights reserved.

1. Introduction

The concept of co-producing hydrogen and electricity using a high temperature fuel cell operating on natural gas is driven by the possibility that hydrogen is more valuable than heat and will become increasingly valuable with the emergence of hydrogen fuel cell vehicles and the required infrastructure for their refueling. Some researchers suggest that this concept will be responsible for 15% of the hydrogen production in 2030 [1]. The term coproduction (sometimes referred to as poly-generation or tri-generation) generally implies increased efficiencies through the production of co-products using one system. The specific case of using a high

temperature fuel cell operating on natural gas to produce electricity and hydrogen has been demonstrated to produce the co-products with high efficiencies [2–5]. Using a solid oxide fuel cell to coproduce hydrogen provides two major benefits: higher cell voltages that lead to higher electrochemical efficiency and the ability to variably produce the co-products – electricity and hydrogen – to meet market demands. Given these possible benefits, it is important to study these systems. In addition, such systems could locally produce hydrogen to avert the emissions and energy penalties associated with distribution of hydrogen to refueling stations. Given these attributes and the likely deployment of hydrogen vehicles in 2015, it is important to study these high temperature fuel cell hydrogen coproduction systems.

Vollmar et al. performed thermodynamic design calculations examining different operating modes of a solid oxide fuel cell (SOFC) hydrogen coproduction system and different overall system

* Corresponding author. Tel.: +1 949 824 1999.

E-mail addresses: jb@nfcrc.uci.edu, jb@apep.uci.edu, jbrouwer@uci.edu (J. Brouwer).

configurations, e.g., some included a proton exchange membrane fuel cell that would operate on the coproduced hydrogen [2]. They showed that high efficiencies could be achieved in a solid oxide fuel cell coproduction system [2]. Leal and Brouwer investigated several solid oxide fuel cell hydrogen coproduction system configurations using thermodynamic analyses [3]. Their results showed that the direct internal reformation (DIR) configuration provided the highest electrical efficiencies and the most hydrogen per unit input of natural gas. Hemmes et al. studied three different operation modes in a direct internal reformation solid oxide fuel cell (DIR-SOFC) hydrogen coproduction system. These researchers concluded that the maximum total efficiency occurs at low fuel utilization regardless of the operating mode selected [4]. Margalef et al. also evaluated several different configurations of a solid oxide fuel cell hydrogen coproduction system using newly developed efficiency definitions [5,6]. Their results were found to be in agreement with Leal and Brouwer [3] in that the DIR (on anode) configuration yielded the highest overall efficiency.

Although previous studies have focused on the optimization of the system configuration and the steady state operation of the system, the study of the dynamic responses of these solid oxide fuel cell hydrogen coproduction systems to various possible perturbations has not yet been performed. The present study will investigate these dynamic system responses by examining the extreme case of a load following DIR-SOFC hydrogen coproduction system servicing the measured demand of a commercial building while storing coproduced hydrogen for later use, e.g., in fuel cell vehicles, industrial processes, or in a stationary proton exchange membrane fuel cell for dynamic dispatch or assistance in load following. Although high temperature fuel cells have yet to be proven as load following devices, some researchers have proposed that solid oxide fuel cells do have inherent transient capabilities that are afforded to them by their electrochemical nature [7].

The current load following analysis was selected to investigate SOFC system transient capabilities for the highly dynamic case of load following a measured building demand, focusing upon the possible dynamic thermal gradients that may be observed in such a system. This highly dynamic case analysis is especially important in a DIR-SOFC hydrogen coproduction system where although the DIR allows high efficiencies and high hydrogen production amounts [3,5] it also results in large thermal gradients within the SOFC. In addition coke formation may occur if high steam to carbon ratios are not dynamically maintained during transient operation [8,9]. Given these issues with DIR operation of SOFCs, it is important to resolve the temperature and species distributions across the SOFC. However, this can require detailed and highly spatially resolved physical modeling which may not be compatible with dynamic system simulation and controls development.

This work describes how a quasi-2-D DIR-SOFC model, which still allows resolution of the temperature and species distributions across the fuel cell, is integrated into a hydrogen coproduction system model, and demonstrates the feasibility of this integrated system's capability to meet the dynamic electrical load of a commercial building while also dynamically producing hydrogen on site for later use or sale (e.g., for vehicles).

2. Approach

This paper aims to investigate the dynamic capabilities of a DIR-SOFC H₂ coproduction system for implementation at a commercial building site. This investigation is accomplished by simulating the DIR-SOFC system as it follows measured building load data for a 24 h period with 3-s resolution. In addition to electrical load dynamics, the system dynamics associated with the hydrogen

collector tank are examined. The dynamic electrical data were measured at a commercial building in the University Research Park near the University of California, Irvine campus on November 8, 2004 [10]. For the purposes of this work, the data were scaled so that a 1 MW SOFC system could continuously follow the building demand.

The hydrogen coproduction system is forced to meet the building load demand completely on its own with the exception of the fuel cell system blower demand. The blower power never exceeded 33 kW during the dynamics of the day (i.e., 3.3% of the maximum power of the system).

3. DIR-SOFC H₂ coproduction system model

The DIR-SOFC H₂ coproduction system model consists of three heat exchangers, a blower, a hydrogen separator, a collection tank, a catalytic burner, and the DIR-SOFC itself (see Fig. 1). The catalytic burner, blower, and hydrogen separator were modeled as single control volumes (bulk models) while the DIR-SOFC and heat exchangers are discretized into multiple control volumes (CV), which allows resolution of spatial distributions of temperature and species concentrations across these components. The system model was constructed in the MATLAB Simulink environment, and the system of ordinary differential equations (ODEs) resulting from the various single control volume system components and the discretization of the DIR-SOFC and the heat exchangers (method of lines) was solved using the numerical ODE solver package, ode15s. See Table 1 for the full specifications of the system.

3.1. Conserved quantities: mass and energy

Pressure is assumed to be constant throughout the system leaving only the conservation equations of energy and mass to be solved for in each control volume, which allows a substantial reduction in computational intensity. This is a reasonable assumption due to low Reynolds number flows and low pressure drops, which previous work has shown to minimally affect model fidelity [11]. With regard to the conservation of mass/species, the following equation is utilized

$$\frac{d}{dt}(NX_{out}) = \dot{N}_{in}X_{in} + R - \dot{N}_{out}X_{out} \quad (1)$$

The conservation of energy equation is shown below

$$\frac{dU}{dt} = \dot{H}_{in} + \dot{H} - \dot{H}_{out} + \dot{E}_{gen} + \sum \dot{Q} \quad (2)$$

The above equations will be solved simultaneously and dynamically for temperature and species concentrations.

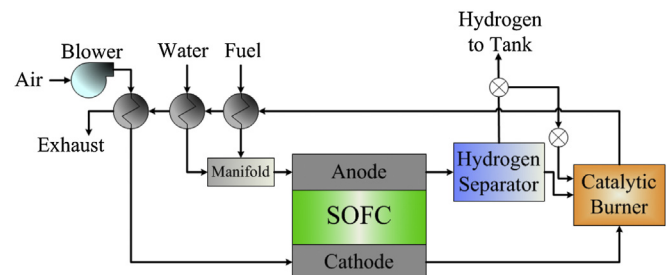


Fig. 1. DIR-SOFC hydrogen coproduction system schematic.

Table 1
Hydrogen coproduction system specifications.

	Value	Units
<i>SOFC parameters</i>		
PEN thickness	1.06	mm
PEN density	5900	kg m ⁻³
PEN specific heat	0.5	kJ kg ⁻¹ K ⁻¹
PEN thermal conductivity	2	W m ⁻¹ K ⁻¹
IC thickness	4	mm
IC density	9000	kg m ⁻³
IC specific heat	0.62	kJ kg ⁻¹ K ⁻¹
IC thermal conductivity	25	W m ⁻¹ K ⁻¹
C1	7509.6	
Cre0	-25.855	
j_o	2000	A m ⁻²
j_l	10,000	A m ⁻²
Cathode channel ht.	2	mm
Anode channel ht.	1	mm
Rib width	0.5	mm
# of flow channels	40	
Cell width	10	cm
Cell length	10	cm
# of Cells	30,000	
Nusselt number	3.8	
<i>HX parameters</i>		
Plate thickness	1.5	mm
Plate density	8500	kg m ⁻³
Plate specific heat	0.6	kJ kg ⁻¹ K ⁻¹
Plate thermal conductivity	2	W m ⁻¹ K ⁻¹
Channel width	0.1	m
Channel height	0.01	m
# Channels – fuel HX	57	
Channel length – fuel HX	2	m
# Channels – Stm HX	129	
Channel length – Stm HX	3	m
# Channels – air HX	1300	
Channel length – air HX	5	m
Nusselt number	5.7	

3.1.1. Heat transfer

The interaction between the phases is through convective heat transfer using Newton's Law of Cooling to model this process.

$$\dot{Q}_{\text{conv}} = hA_i(T_s - T_f) \quad (3)$$

The convection heat transfer coefficient, h , is determined using the equation for the Nusselt number with local properties. The Nusselt numbers for the typical dimensions of the gas channels in the fuel cell and the gas channels in the heat exchanger are 3.8 and 5.7, respectively [12].

$$h = \frac{k}{D_h} \text{Nu} \quad (4)$$

The thermal conductivity of the gas is calculated using the following approximation:

$$k = \sum X_i k_i(T_{\text{out}}) \quad (5)$$

Radiation is assumed negligible throughout the model, which is a reasonable assumption for a planar SOFC that has facing surfaces with very similar temperatures. The solid CVs interact energetically through conductive heat transfer modeled using Fourier's Law

$$\dot{Q}_{\text{cond}} = kA \frac{(T_h - T_l)}{L} \quad (6)$$

3.2. Solid oxide fuel cell

The DIR-SOFC stack is sized for a maximum power output of 1 MW at 0.7 V and 85% fuel utilization. The DIR-SOFC stack is modeled with the assumption that a single cell is a representative of all the cells in the stack. While this assumption does not allow the model to capture some of the major stack spatial variations in temperature, species, or current that can occur during large transients, the discretization of the single cell does resolve these variations in the major flow direction(s) of the stack. This is the direction in which the most significant spatial variations typically occur within a stack. The current approach allows some assessment of the severity of thermal and concentration gradients during transients with sufficient simplicity to retain computational efficiency. This assumption is common in the literature [13–20]. The DIR-SOFC single cell model considers the co-flow configuration and models only one complete fuel and oxidant channel under the assumption that one channel is representative of the rest due to the symmetry of the co-flow configuration.

The cell is then discretized in the flow direction to resolve local current production, species concentrations, temperature, etc. Each discretization in the flow direction results in a set of four new control volumes (Anode, IC, Cathode, PEN). These sets are referred to as nodes. Sensitivity analyses on the number of nodes needed for accurate description of cell processes was determined in a previous publication [21]. The number of nodes that sufficiently reduced computational intensity without loss of much fidelity was 24 nodes. The various other assumptions associated with the fuel cell model are listed below.

- 1) The fuel cell is well insulated such that heat loss from the cell is negligible.
- 2) The flow in the fuel cell is laminar.
- 3) Pressure drops are negligible [11].
- 4) The gases are ideal and incompressible.
- 5) Radiation heat transfer is negligible [22,23].
- 6) Conduction along the PEN is negligible since conduction through the interconnect dominates.
- 7) Coking is negligible due to the high steam to carbon ratio used in the following analyses [8,9].
- 8) The water–gas-shift reaction is assumed to be in equilibrium.
- 9) Both electrodes exhibit high enough conductivity that it is assumed that both are an equi-potential surface.
- 10) Only hydrogen participates in the electrochemical reaction at the anode.
- 11) The electrochemistry is rapid such that the rate of reaction is proportional to the current.

Further details regarding the DIR-SOFC model such as the polarization and reformation models are described in previous publications [21,24]. In summary, local Nernst potential, activation, ohmic and concentration polarizations are determined concurrently with kinetic rates for steam reforming and water–gas-shift chemistry. This modeling methodology is similar to those presented in prior publications [13–20,25,26]. The modeling methodology has also been shown to reasonably predict operation of experimental systems including complete integrated systems and single cell experiments [13,14,17,19,25,26].

3.3. Heat exchangers

The heat exchanger model simulates a counter flow plate heat exchanger. For each heat exchanger, only one plate is modeled with its corresponding hot and cold gas streams. This methodology is

based on the assumption that the single plate modeled is representative of the rest of the plates within the heat exchanger. The flows within the heat exchangers are laminar given the size and number of channels. The representative plate is further discretized into five nodes. Within each control volume, mass and energy are conserved, and the appropriate heat fluxes are accounted for.

The heat exchangers were sized such that for steady operation of the system at 818 kW and a fuel utilization of 78% without burning the collected hydrogen, the heat exchangers would supply inlet streams to the fuel cell at 1023 K.

3.4. Catalytic burner

The catalytic burner model assumes that complete combustion of the anode off gases will occur. However, the burner model is capable of rendering a solution for situations in which there is not sufficient oxygen available for complete combustion of all the fuel. No equilibrium calculation is performed because it only slightly changes temperatures and species compositions while significantly increasing computation time. Conservation of energy is applied such that the exit temperature (and combustor temperature) can be calculated. The combustor is a single control volume bulk model that is adiabatic.

3.5. Hydrogen separator

The hydrogen separator is also modeled as a single control volume, bulk model. It simply removes all the hydrogen from the incoming stream, which is then routed to the storage tank. When the tank is full, this separated hydrogen is re-routed to the combustor. Another strategy could have been to turn off the separator, but in practice, this would not allow any fast dynamic switching back to the production of hydrogen for filling the tank since it would take some time for the separator to become operable again. For example, ion transport membranes (a type of hydrogen separator) have high operating temperatures and hence require time to heat up. Therefore, the current strategy for keeping the hydrogen separator in operation at all times was chosen. After the hydrogen is removed for collection, an equilibrium calculation is then performed to determine the species compositions that enter the combustor. Conservation of energy is used to calculate the exit temperature of this mixture.

3.6. Tank

The tank model simply accounts for how much hydrogen has been collected or removed. The tank is sized so that it can store 20 kg of hydrogen, which could provide fuel for fuel cell vehicles, industrial processes or a stationary fuel cell that could assist the DIR-SOFC system with load following. This tank would hold sufficient fuel to supply a 100 kW fuel cell at full load for 6.7 h or fill approximately 4 fuel cell vehicles.

3.7. Blower

The blower is dynamically modeled by assuming isentropic operation with an efficiency of 85% and performing a dynamic torque balance on the shaft of the blower. This results in the following equations, respectively:

$$P_{\text{blower}} = \frac{1}{\eta_{\text{blower}}} \frac{\gamma R T_{\text{amb}}}{\gamma - 1} \left[\left(\frac{P_{\text{out}}}{P_{\text{amb}}} \right)^{\gamma-1/\gamma} - 1 \right] \quad (7)$$

$$J\omega \frac{d\omega}{dt} = P_{\text{motor}} + P_{\text{blower}} \quad (8)$$

The blower power is determined using the first equation. The flow rate and exit pressure were determined from the performance curves of an actual 5000 CFM blower manufactured by Dresser Industries, Inc. (RCS-J Frame 832). A linear approximation was used to describe the regions for which there were no data (below 1000 CFM). Application of the conservation of energy allowed the determination of the temperature of the air exiting the blower. Additionally, for simplification purposes the blower was not powered by the fuel cell directly rather it was assumed to be powered by the utility grid.

Detailed specifications of each component of the SOFC system model are provided in Table 1.

3.8. Control schemes

3.8.1. Fuel flow rate controller

The fuel flow rate is controlled using the current to determine the amount of fuel that is needed within the anode compartment [27]. The following equation governs the fuel flow rate:

$$\dot{N}_{\text{fuel}} = \frac{I}{(X_{\text{CH}_4} + X_{\text{CO}} + X_{\text{H}_2}) \cdot U_f \cdot n \cdot F} \quad (9)$$

A fuel valve actuation and flow delay of 2 s has been modeled in a manner that resembles the physical delay between the fuel flow rate command at the control valve and the actual fuel flow that enters the fuel cell.

The fuel utilization was controlled differently depending upon whether or not the hydrogen storage tank was full. This is because in a H₂ coproduction system, the hydrogen production rate is highest at a low fuel utilization; therefore, when the system operator wants to collect hydrogen a low fuel utilization is desired [4]. Before the tank is full, the fuel utilization is set for a relatively low fuel utilization value of 72%. This was needed in order to ensure that the combustor temperature would stay below 1300 K. If very low fuel utilizations were used (<72%), the result would be very high combustor temperatures due to the excess fuel in the anode off gas, which could potentially damage the combustion catalyst or the first heat exchanger in the system. After the tank is full, excess fuel in the exhaust is not desirable since it cannot be collected and stored, therefore, a higher utilization is desired. The higher utilization selected for this work is 85%. Once the tank is within 1 kg of being full, the fuel utilization is ramped to 85% within 30 s.

3.8.2. Air flow rate controller

The air flow rate is controlled by driving the manipulated variable (the blower motor power) to a value such that the air flow through the fuel cell provides sufficient convective cooling for maintaining SOFC temperature. In particular, the controlled variable is the cathode exhaust temperature, which is controlled to remain at 1173 K and which well controls overall SOFC temperatures for this co-flow configuration. The controller used in this work is a cascade controller adapted from Ref. [16].

The feed forward controls were calibrated such that during operation of the system at 818 kW and a fuel utilization of 78%, the cathode exhaust temperature is within 0.1 K of 1173 K. The air flow rate controller PI constants were determined by simply choosing the largest possible gains for which the system model would still converge. No integral or derivative terms were included. This process determined $K_p = 35$ and $K_{rpm} = 7$, neither of which have been determined to be optimal.

3.8.3. Collection tank controls

There is additional control on the hydrogen fill tank. As the tank nears the maximum fill level (within 1 kg of full), the fuel utilization

is increased from its minimum value to the maximum value of 85% within 30 s. Once the tank is then completely full (20 kg), the valve to the tank shuts while another valve opens routing the separated hydrogen to the combustor. Another strategy could have been to turn off the separator, but in practice, this would not allow any fast dynamic switching back to routing hydrogen to the fill tank since it would take some time for the separator to become operable again. For example, ion transport membranes have high operating temperatures hence require time to heat up. Therefore, the current strategy for keeping the hydrogen separator in operation at all times was chosen.

4. Results and analysis

Fig. 2 shows the scaled commercial building that was measured in the University Research Park near the University of California, Irvine campus on November 8, 2004 [10]. One should notice two significant dynamic changes in the building load that are associated with the start-up and shut-down of the heating, ventilation, and air conditioning (HVAC) systems of the building. In addition, instantaneous (3-s resolution) dynamic variations of 100 kW (10% of full load) are common in the building demand data. In addition to these electrical dynamics, two other dynamics associated with the filling of the hydrogen storage tank occur over the period of 24 h. The fuel utilization is increased when the hydrogen storage tank reaches 19 kg (size of tank 20 kg), and the hydrogen separated in the separator is re-routed from filling the hydrogen storage tank to the combustor once the tank is full.

The dotted vertical lines in Fig. 2 are placed exactly at the times when these large dynamics began: the first is the large electrical load increase; the second is the fuel utilization increase as a result of the collection tank approaching full; the third is the re-routing of the separated hydrogen out of the separator to the combustor when the tank is full; and the last is the large electrical load decrease. See Table 2, which specifies the times and durations of these transients.

4.1. System wide results

4.1.1. SOFC inlet/outlet, combustor, and HX exit temperatures

Fig. 3 shows the SOFC inlet and outlet temperatures. The SOFC inlet temperatures are also the exit temperatures from the cold side of the heat exchangers. The SOFC inlet temperatures are higher than the specified 1023 K because the heat exchangers were sized for a specific set of operating conditions ($P = 818$ kW and $U_f = 78\%$ with the separated hydrogen out of the separator stored). Since the fuel utilization is lower than what the HXs were sized at, the combustor temperature is much higher than during the HX calibration, which results in the higher inlet temperatures. Additionally, at the lower power, there are lower flow rates through the HXs, which results in a longer residence time of the fluid within the heat exchanger since it is sized for higher flow rates, and thereby increases the inlet temperatures to the SOFC.

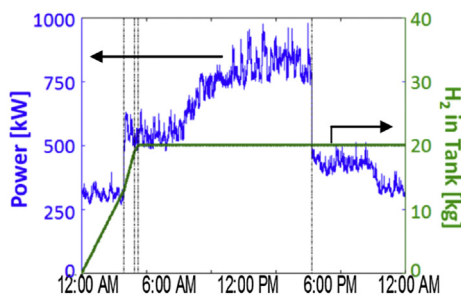


Fig. 2. SOFC diurnal power and hydrogen collection profiles.

Table 2
Times and durations of the large dynamics of the system.

Dynamic	Time	Time [ks]
First electrical dynamic		
Start	3:05:24 AM	11.124
Stop	3:15:06 AM	11.706
Δt [mm:ss, ks]	9:42	0.582
Fuel utilization dynamic		
Start	3:54:15 AM	14.055
Stop	3:54:45 AM	14.085
Δt [mm:ss, ks]	0:30	0.03
Tank full dynamic		
Start	4:11:54 AM	15.114
Second electrical dynamic		
Start	5:04:18 AM	61.458
Stop	5:04:24 AM	61.464
Δt [mm:ss, ks]	0:06	0.006

The SOFC exit temperatures remain near 1173 K, and in fact the anode and cathode exit temperatures are not discernible from each other in Fig. 3. This is because in the co-flow configuration the anode and cathode gases flow along the cell in the same direction and exit on the same side of the cell. The anode and cathode exhaust temperatures are also nearly the same as the maximum PEN temperature for the same reason (see Fig. 10). The cathode exhaust temperature is primarily controlled through manipulation of the air flow rate.

Fig. 4 displays the combustor temperature, which is the inlet to the hot side of the first (fuel) heat exchanger. The other temperatures in Fig. 4 are the exit temperatures of the hot side of the respective heat exchanger but are also the inlet temperatures of the hot side of the next heat exchanger in the series. It is interesting to note that the combustor temperature in Fig. 4 significantly overshoots the maximum temperature of 1300 K after the last large electrical dynamic perturbation of the evening. Recall that this maximum was specified in order to protect the materials in the catalytic combustor as well as in the first heat exchanger. This large overshoot results from the control on the air flow rate that tries to maintain the cathode exhaust temperature at 1173 K while the SOFC power drops to follow the quickly decreasing load. The decrease in SOFC power has a requisite decrease in heat release resulting in a decrease in SOFC exit temperatures. This instigates a

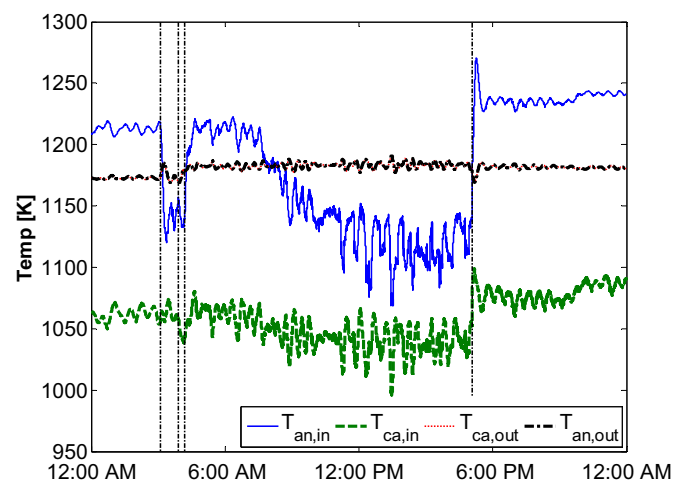


Fig. 3. SOFC inlet and outlet temperatures while following the diurnal building load.

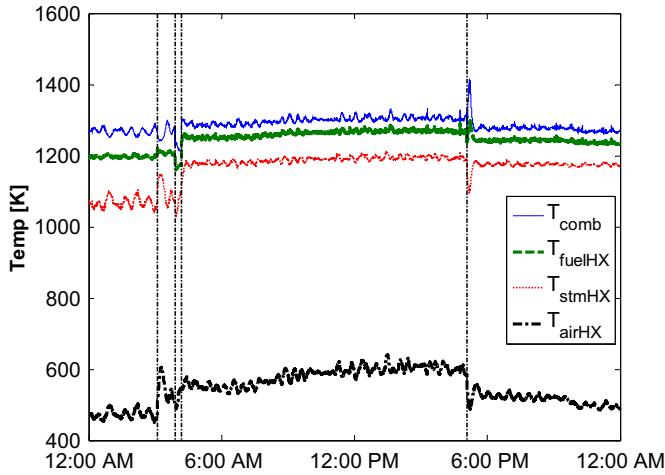


Fig. 4. Combustor and heat exchanger exit temperatures while following the diurnal building load.

large drop in air flow rate as evidenced by the large increase in air utilization, shown in Fig. 7. The decrease in air utilization means less excess oxygen in the cathode exhaust, which causes an increase in combustor temperature because the combustion conditions move closer to stoichiometric. Both the excessive combustor temperature and low air utilization are unacceptable and demonstrate that the current control strategy needs improvement. Major improvements could be made with regard to the predictability of these large load transients where the DIR-SOFC system could prepare in advance for the large transient, or the PID control constants could be made more robust.

During the first large electrical dynamic, the anode inlet temperature decreases by about 100 K. This reduction can be attributed to two occurrences. One is to note that as the load is increased, higher flow rates ensue, which results in flow rates closer to those observed when the HXs were calibrated for 1023 K inlet temperatures. The higher flow rates reduce the residence time of the gas within the HX decreasing heat transfer to the gas. Secondly, the air utilization and the cathode exhaust temperature in Fig. 8 shows that as the load was increased, $T_{ca,out}$ began to increase due to the increased heat generation. However, once the air flow rate controller sensed the $T_{ca,out}$ increasing, it began to ramp the speed

of the blower up dramatically as indicated by the decrease in air utilization. This increased air flow rate then cooled the combustor down about 50 K, which led to the decreased heating potential for the SOFC inlet gases (see Fig. 6 which shows the anode inlet temperature, combustor temperature, and the exit temperature from the hot side of the fuel HX and steam HX).

It is interesting to note how the hot stream exit temperature from the fuel HX does not vary much after the first large electrical dynamic. This is once again a result of the increased fuel flow rate and the effect on residence time and heat transfer described above. As the fuel flow is increased due to the load increase, the residence time of the fuel within the heat exchanger is shorter. The decreased residence time leads to decreased heating, which allows T_{fuelHX} to remain the same although T_{comb} has decreased. A decreased heating potential is acceptable since less heating is possible. The same idea is applicable to the steam and air heat exchangers. With these heat exchangers, the increased flow rates cause a decrease in the possible heating of the inlet gases, which allows the exit temperatures of the hot streams to increase.

Examining the fuel utilization dynamic next, it is easy to understand why the temperatures dip soon after the building load increase dynamic. This is due to the decreased heating value of the anode off gas entering the hydrogen separator and finally the combustor since more hydrogen is now being consumed within the SOFC itself for power production. These temperatures soon rebound once the tank becomes full and the separated hydrogen out of the separator is re-routed to the combustor (Fig. 6).

After the fuel utilization and hydrogen re-route dynamic, the inlet temperatures approximately follow the profile of the electrical load, inversely. This makes sense because the HXs were calibrated for a power of 818 kW, and as the power nears this power output, the flow rates increase leading to less heat transfer to the inlet gases. However, the anode inlet temperatures never quite reach their calibrated value of 1023 K. This is due to the higher utilization (85%) seen in this part of the day than in the HX calibration (78%).

The second electrical dynamic is very fast lasting only several seconds. The dynamic causes a rapid increase in the inlet SOFC temperatures. Even the increase of the cathode inlet temperature is fairly large. This increase is due to the decreased flow rates needed at the lower power and the excess fuel available to the combustor immediately after the electric load reduction transient. The electrical transient happens quickly while the fuel flow rate cannot be changed as quickly (delay of several seconds), which results in the

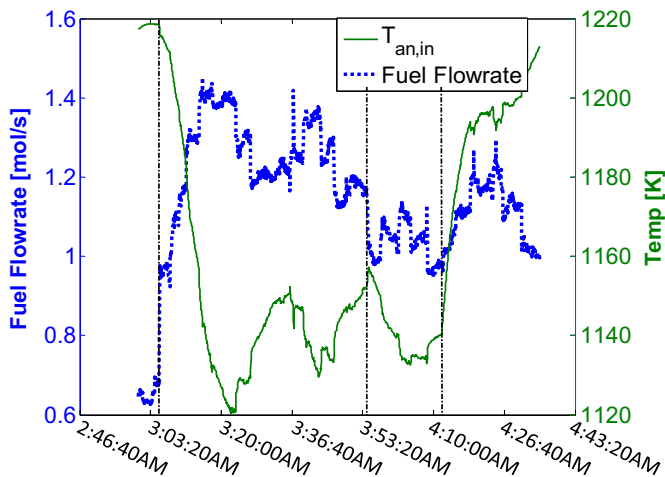


Fig. 5. Zoomed view for the morning dynamics of the anode inlet temperature and the fuel flow rate.

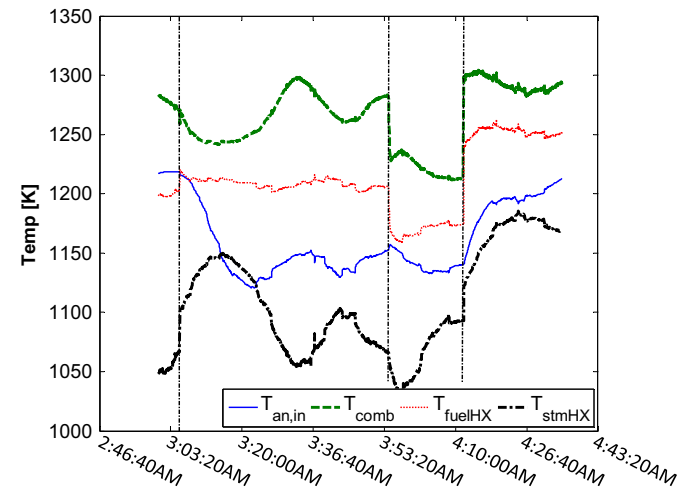


Fig. 6. Zoomed view for the morning dynamics of the anode, combustor, and the exit temperatures from the hot side of the fuel and steam heat exchangers.

excess fuel in the SOFC anode exhaust during a power decrease. This excess fuel in the SOFC exhaust directly explains the large increase in the combustor temperature and fuel HX hot side exit temperature. What is more interesting is the decrease in the hot stream exit temperatures of the steam and air heat exchangers. The reasoning behind this is similar to that when these temperatures increased after the previous load increase dynamic. As the combustor temperature increased, the steam and air flow rates decreased, but these decreased flow rates increase the residence time of the gases, which allowed much more effective heating to occur and thereby decreased the hot stream exit temperatures for the air and steam HXs.

4.1.2. Utilizations

Fig. 7 displays the fuel utilization transient well. The fuel utilization shows some oscillation about the desired setpoint due to the delay between when the fuel flow is increased and the time at which the fuel reaches the SOFC. The delay, however, may cause oscillations in the fuel utilization that may be too high for the SOFC. During the oscillations, the fuel utilization surpasses 85% frequently, which in a practical situation, could mean that within the SOFC itself there could be regions with even higher utilizations that could degrade the cell performance (e.g., by anode nickel oxidation). Therefore, it may be necessary to decrease the maximum fuel utilization down to 80%.

The air utilization oscillates more than the fuel utilization since the air flow rate is being manipulated such that $T_{ca,out}$ is maintained. These oscillations appear larger earlier in the day when the power and fuel utilization are low. After the first three transients, the severity of these oscillations dampens with the exception of the spike in U_a during the large electrical load decrease at the end of the day. Additionally after the first three transients, the air utilization decreases to a much lower average value than before the respective transients. The air utilization also surpasses 50% several times throughout the day, which can be detrimental to the cell performance. Both the large oscillations and spikes past 50% can be attributed to delays between when the air flow is increased and when the increased air flow actually begins to decrease the controlled variable, $T_{ca,out}$.

As previously mentioned, the primary factor involved in all of the large oscillations (spikes) of the air utilization is the delay between the time at which the air flow rate controller acts on the manipulated variable, blower power, and the time at which the controlled variable, $T_{ca,out}$, responds (due to the large thermal mass

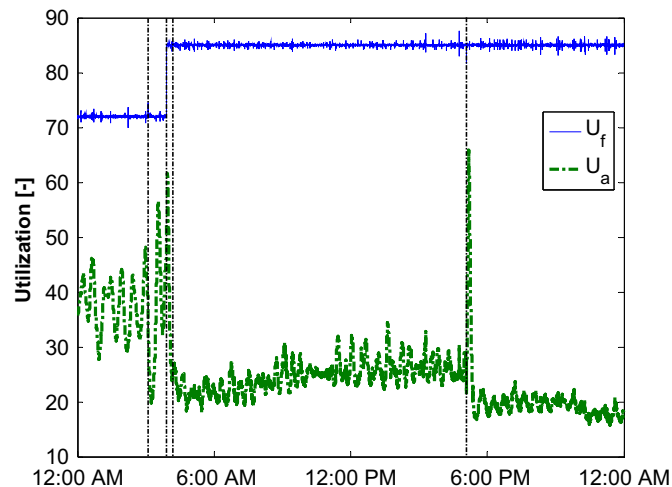


Fig. 7. Fuel and air utilizations while following the diurnal building load.

of and the complex set of chemical and electrochemical reactions and heat transfer that occur in the fuel cell). However, before the second transient (U_f increase), there are additional factors at work that increase the delays observed and increasing the oscillations. Before the first transient, the system is operating at very low power ($\sim 30\%$ of full), which results in much lower air flow rates than those seen while operating at full power or even half power because there is less heat generation. The low fuel utilization before the second transient results in even less heat generation within the fuel cell, thereby further decreasing the convective cooling needed by the SOFC from the air flow. Additionally, when the hydrogen in the anode off gas is being collected in the hydrogen storage tank, the air flow rates are even lower due to the lower Btu content of the gas entering the combustor. However, at these turned down operating conditions, the lower air flows, which have much less cooling potential, result in even longer delays than higher air flow rates. This results in the need for larger increases or decreases in the air flow rate in order to maintain $T_{ca,out}$.

By examining Fig. 8 the delay can be observed. As the power increases, the cathode exhaust temperature begins to rise because of the increased heat generation due to the increased electrochemical activity. As soon as this rise is sensed by the air flow rate controller, it increases the air flow rate by increasing the blower power. This increased air flow rate is evidenced by the decrease in air utilization. However, the increased air flow rate does not immediately cause the controlled variable ($T_{ca,out}$) to decrease due to the delay. This resulted in the controller increasing the air flow rate even more since the rise in $T_{ca,out}$ continued. A better controller may have led to much smaller increases. All of this was manifested as the spike downward in the U_a and the spike upward in $T_{ca,out}$ right after the first electrical dynamic. Had there been no delay or had the controller gains been better optimized, these spikes could have been mitigated somewhat. The same thing occurred in the second electrical dynamic, however, since it was a power decrease, everything was inverted.

During the fuel utilization transient, the cathode exhaust temperature decreased which led to an increase in air utilization, but it is hard to discern whether or not it was due to the fuel utilization increase or the power decrease that happened right after it. However, after looking at the PEN temperatures in Fig. 10, it is easy to see that the increase in fuel utilization causes an increase in the maximum PEN temperature. This is just further evidence of the delays associated with controlling the cathode exhaust temperature. The fuel cell is heating up while the cathode exhaust is

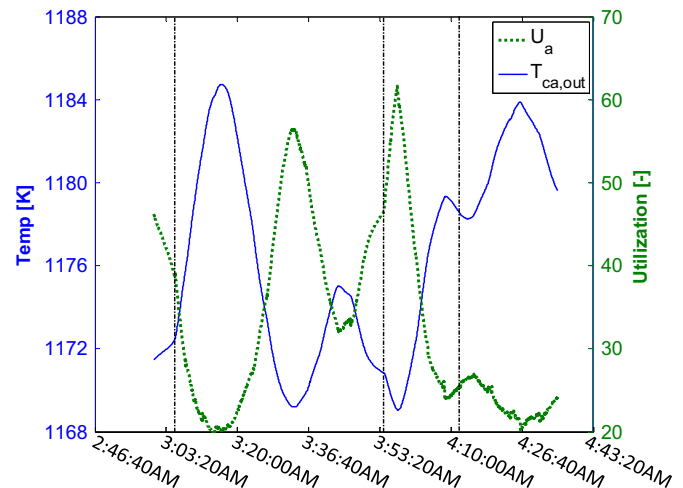


Fig. 8. $T_{ca,out}$ and air utilization during the first three dynamics.

actually cooling down, which causes the air flow rate to decrease even though the cell is heating up. Controlling the PEN temperature itself might result in better control, however, it would be very difficult to measure that temperature in a practical application.

After the hydrogen re-route dynamic, the cathode exhaust continues to heat up, due to the combination of the increase in the temperature of the combustor and the increase in power. The increase in power output results in the increase of $T_{ca,out}$, but the increase in the inlet temperatures makes it harder for the air flow rate to cool the cell (Fig. 3). The cathode exhaust temperature follows the increase in load nicely (Fig. 9). During this time the air flow rate is ramped up even more so as to account for this combination of heat sources (Fig. 8). Additionally, the PEN temperature distribution across the cell during the third dynamic (hydrogen tank shut off) shows that the re-route of the separated hydrogen out of the separator to the combustor has little effect on the SOFC itself (Fig. 10).

The large electrical load decrease at the end of the day is very abrupt (several seconds), which causes a large increase in the fuel utilization due to the delay between the action of the manipulated variable and the response of the controlled variable. This load decrease showcases this delay the best since the power is decreased so rapidly. To summarize, two factors were significant in the analysis of the air utilization: the delays inherent within the system and the system turndown's effect on these delays. As the system was turned down, the delays were exacerbated, which led to increased oscillation.

4.1.3. PEN temperatures

Fig. 10 displays the PEN temperatures. The maximum PEN temperature is very similar to the cathode and anode exhaust temperatures and remains near 1173 K because of the control on the cathode exhaust temperature. It is interesting to note how the minimum PEN temperature follows the shape of the power output only inverted. Since the maximum PEN temperature remains near constant, ΔT_{PEN} follows the shape of the power output. During the fuel utilization transient, ΔT_{PEN} drops a little as the minimum PEN temperature increases due to the increased heat generation. During power increases the minimum PEN temperature decreases as a result of two things: the increased air flow rate and the increased fuel flow rate, which leads to more endothermic SMR reactions (see Intra-cell results section). This decrease translates into an increase in the ΔT_{PEN} , which is why it follows the power profile of the system

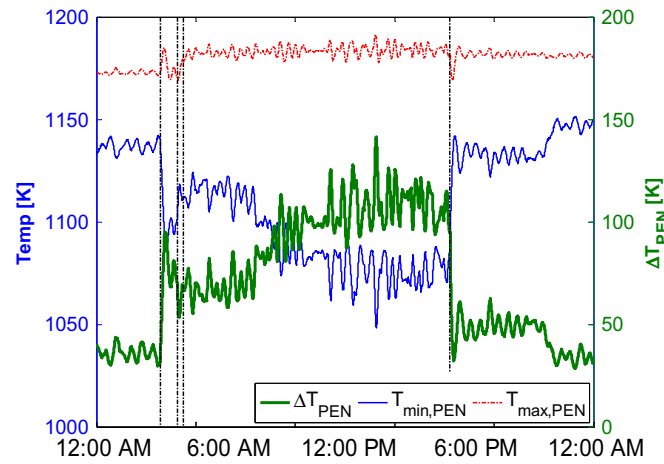


Fig. 10. PEN temperatures while following the diurnal building load.

to a degree. ΔT_{PEN} is also a maximum when the power is a maximum for the same reason. Overall, the PEN temperatures and the cross cell PEN temperature differences during these significant transients with less than optimal controllers are still maintained quite well within limits that are typically acceptable in the literature (i.e., $\Delta T_{PEN} < 200$ K, and $T_{max,PEN} < 1200$ K).

4.1.4. Efficiencies

Several efficiencies are defined here: electric, electrochemical, mixed/total, and reformation. The mixed total efficiency attempts to assess the efficiency of the entire system by including the electrical and stored chemical energy produced by the system.

$$\epsilon_{electric} = \frac{\dot{W}_{elec} - P_{blower}}{\dot{N}_{CH_4,in} M_{CH_4} (LHV)_{CH_4}} \times 100 \quad (10)$$

$$\epsilon_{electrochem} = \frac{V_{cell}}{E_0} \times 100 \quad (11)$$

$$\epsilon_{mixed,total} = \frac{\dot{W}_{elec} + \dot{N}_{H_2,collector} M_{H_2} (LHV)_{H_2}}{\dot{N}_{CH_4,in} M_{CH_4} (LHV)_{CH_4}} \times 100 \quad (12)$$

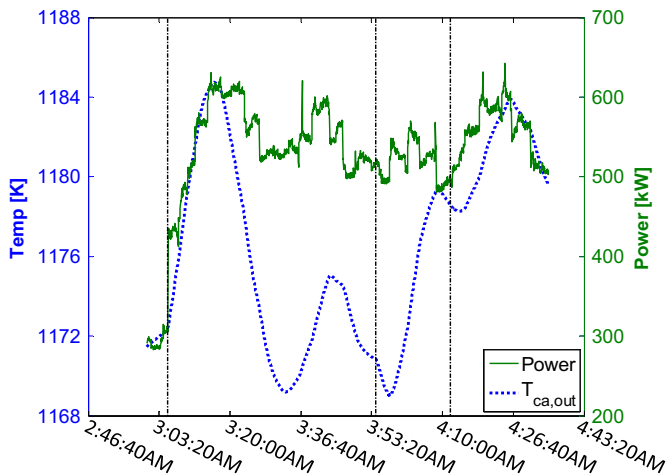


Fig. 9. Cathode exhaust temperature and SOFC power output during the first three dynamics.

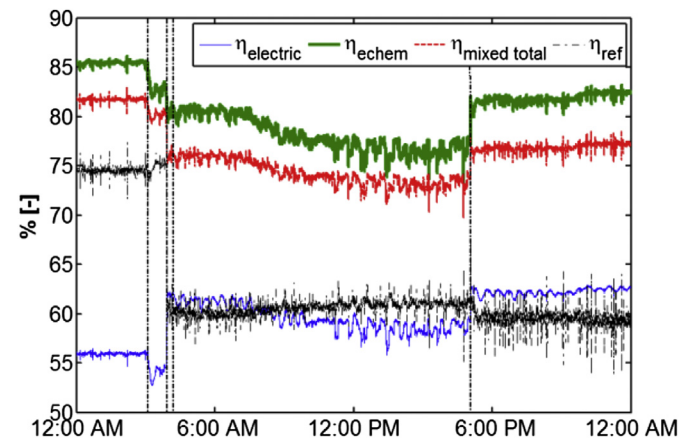


Fig. 11. Various efficiencies while following the building diurnal load and co-producing hydrogen.

$$\epsilon_{\text{ref}} = \frac{\dot{N}_{\text{H}_2, \text{collector}} M_{\text{H}_2} (\text{LHV})_{\text{H}_2}}{\dot{N}_{\text{CH}_4, \text{in}} M_{\text{CH}_4} (\text{LHV})_{\text{CH}_4} - \frac{\dot{W}_e}{\epsilon_{\text{echem}}}} \times 100 \quad (13)$$

Fig. 11 shows these efficiencies as they change throughout the day. It is important to note here that the hydrogen separator still separates hydrogen from the anode off gas when the tank is full in order to remain ready for any pending quick dynamic need to produce hydrogen for storage. When the tank is full, this separated pure hydrogen is not collected but re-routed to the combustor. Therefore, one should not expect the “mixed, total” and “reformation” efficiencies to become equal to the electric efficiency and zero, respectively in Fig. 11, once the tank becomes full (third dashed line). Rather, these efficiencies reflect the approach of always separating hydrogen from the anode off gas and thus always producing hydrogen. This presentation does not penalize the system for having too small of a tank by showing the possible “mixed, total” and “reformation” efficiencies had there been a larger tank (for example). The electric efficiency may seem very high, however, one must remember that the number of cells in the fuel cell stack were chosen such that 1000 kW would be produced at a voltage of 0.7 V and a utilization of 85%. This corresponds to a current density of about 480 mA cm^{-2} . For most of the day the building load stays far below this peak power allowing higher voltages, which leads to higher efficiencies.

When comparing these operating points to others in the literature (e.g., 0.65 V at $\sim 500 \text{ mA cm}^{-2}$) for similar fuel utilizations, it becomes clear that the electrochemical performance is better here [28], but the electrochemical performance is still below that of the highest performing cells in the Solid State Energy Conversion Alliance (SECA) program [29]. The electrical and electrochemical efficiencies follow the inverted shape of the power output. However, they react differently to the fuel utilization increase. The electrical efficiency increases while the electrochemical efficiency decreases. The electrical efficiency increases because at a higher fuel utilization more fuel is electrochemically reacted to produce electricity rather than exhausted in the anode off gas. On the other hand, a lower fuel utilization creates a higher electrochemical efficiency because polarizations are reduced due to the excess fuel available in the anode. This is supported by previous work where it was shown that at higher fuel utilizations, higher electric and lower electrochemical efficiencies occur [30]. The reformation efficiency is similar to typical steam reformer efficiencies (65–75%). When the fuel cell is running at low fuel utilization (72%) at the beginning of the day, the efficiency is at the high end of the typical steam reformer efficiency range. If this low fuel utilization could be decreased further this efficiency could be increased further, however, decreasing the fuel utilization more would lead to excessive combustor temperatures in this particular system. The mixed total efficiency approaches a maximum near 82%.

Operation in hydrogen collection mode generates higher efficiencies than in the electricity only mode simply because the excess fuel in the exhaust is recovered while the fuel cell is able to synergistically operate at a higher electrochemical efficiency due to the lower fuel utilization. In fact, from Fig. 11 it appears that the operating point that produces the highest mixed, total efficiency is low fuel utilization and low power as indicated by the highest mixed, total efficiency in the early morning where the power and utilization were lowest. This corresponds to the operating point of highest electrochemical efficiency and hydrogen production efficiency, but lowest electrical efficiency. This all suggests that while co-producing hydrogen it is most efficient to operate at a condition where electrochemical and hydrogen production efficiencies are maximized (low fuel utilization and power).

Additionally, one should realize again that the use of lower utilization may also bump up this mixed, total efficiency even

higher. This lower utilization would increase the electrochemical and hydrogen production efficiencies thereby increasing the mixed, total efficiency.

4.1.5. Hydrogen separator flows

Fig. 12 plots several mass flow rates: the pure hydrogen that has been separated from the anode off gas in the separator and the carbon monoxide and hydrogen left after the separation. The pure H_2 stream that is separated from the anode off gas is collected until the tank becomes full (third dashed line). Recall that once the tank is full, the separator continues to operate, and this pure H_2 stream is re-routed to the combustor. Fig. 12 also shows the flow rates of the mixed CO and H_2 stream that is left after separation (recall an equilibrium calculation is performed after the separation to determine the left over species, so there is a small amount of hydrogen that is not separated out and is denoted as “ H_2 not separated” in Fig. 12). These plots follow the power output profile of the system. This makes sense in that as the power is increased more fuel is needed which means more excess fuel will be available in the exhaust stream. At increased power, increased H_2 and CO mass flow rates are seen, and at increased fuel utilization, decreased H_2 and CO mass flow rates are seen. Both of these results have been shown to be the case in previous work [30]. Also note that when the DIR-SOFC system is running at lower fuel utilization before the tank is full there is more H_2 and CO available.

4.2. Intra-cell results

This section will focus on the properties within the SOFC during the day, i.e., the temperature and species concentrations will be examined.

4.2.1. First dynamic

Fig. 13 shows that the PEN temperature distribution changes considerably during the large electric load increase in the morning. This was also evidenced in Fig. 10 where the minimum PEN temperature decreased as this dynamic was encountered. The maximum PEN temperatures also change but not as much due to the control of the cathode exhaust temperature. Fig. 13 illustrates nicely how as the power of the SOFC is increased, the latter half of the cell begins to heat up which commences a higher air flow rate to try and bring this temperature down. This increased air flow provides the most cooling near the inlet as shown in Fig. 13. It is also interesting to note how the increased fuel flow rate due to the power increase also contributes to the cooling of the cell in the first

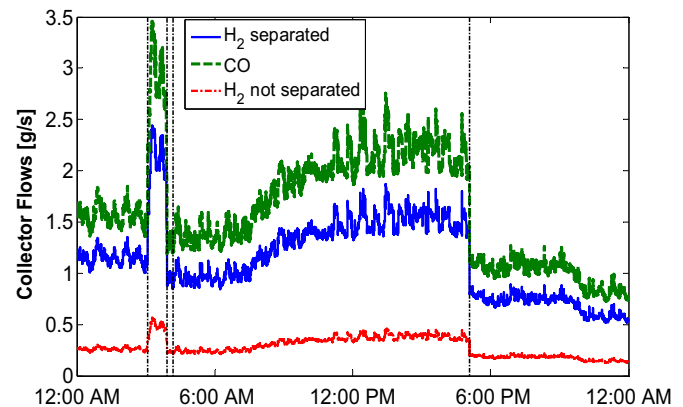


Fig. 12. Hydrogen separator exit stream flow rates while following the diurnal building load.

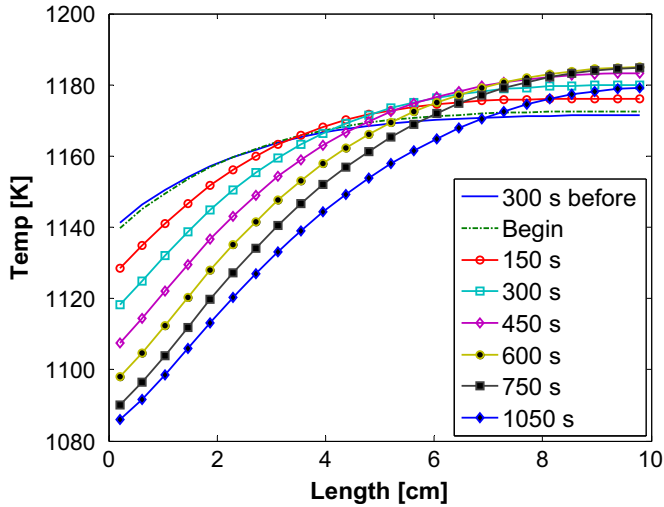


Fig. 13. PEN temperature distribution during the first large dynamic of the day.

few centimeters through increased endothermic steam methane reformation reactions.

Fig. 14 shows how the increased fuel flow rate has led to higher concentrations of methane within the first 2 cm of the cell. The increased methane concentrations were also caused by a decrease in the temperature near the inlet, which in turn caused a decrease in the rate of the SMR reactions. However, although the rate of the SMR reactions decreased, the total number of SMR reactions increased, which contributed to more endothermic cooling near the cell inlet. The decrease in reaction rate simply led to a slower overall conversion of methane.

The current density distribution shown in Fig. 15 looks as expected with the highest current density occurring where the most hydrogen is available in the fuel channel (see Fig. 16). The peak of the current density also moves as the hydrogen concentration peak moves. The evolution of the distribution during the transient is also as expected: as the power is increased the current density is also increased.

The hydrogen concentration distribution became flattened during this dynamic. The peak decreased as the power was increased, and the hydrogen concentrations near the middle of the fuel channel increased, although the concentrations near the exit

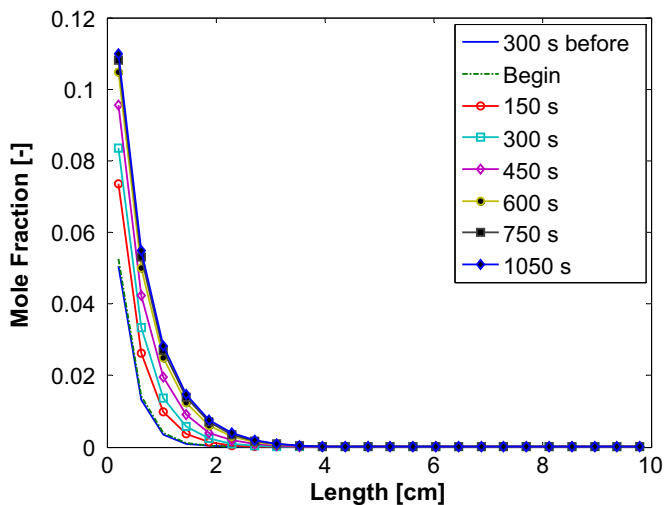


Fig. 14. Methane concentration distribution during the first large dynamic of the day.

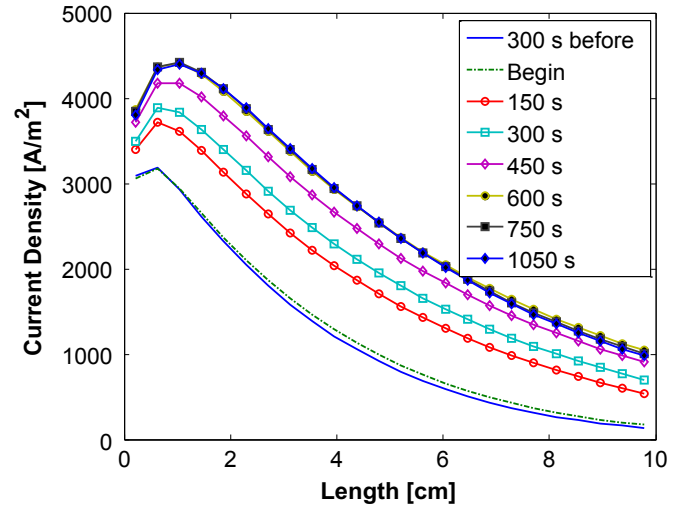


Fig. 15. Current density distribution during the first large dynamic of the day.

remained close to the same. The peak also moved down the channel because as the fuel flow rate increased the rate of the SMR reactions could not continue to reform all the methane so quickly and temperatures were lowered. This affected electrochemical rates and SMR rates leading to higher concentrations of methane farther down the fuel channel and higher concentrations of hydrogen further down the fuel channel. This also explains the lower hydrogen concentrations at the cell inlet.

To summarize the following discussions, the power increase led to an increase in the maximum PEN temperature because of increased heat generation. This in turn caused an increase in the air flow rate and fuel flow rate. Both of these flow rates contributed to the decrease in the minimum PEN temperature, but the air flow rate probably played the larger role. As this minimum PEN temperature decreased, it led to a lower rate of reaction for the SMR.

4.2.2. Second dynamic

The second dynamic perturbation was the fuel utilization increase from 72% to 85%, which occurred as the hydrogen tank become full. Separating the contributions from the fuel utilization dynamic and the continuous changes in power is facilitated by the inclusion of Table 3.

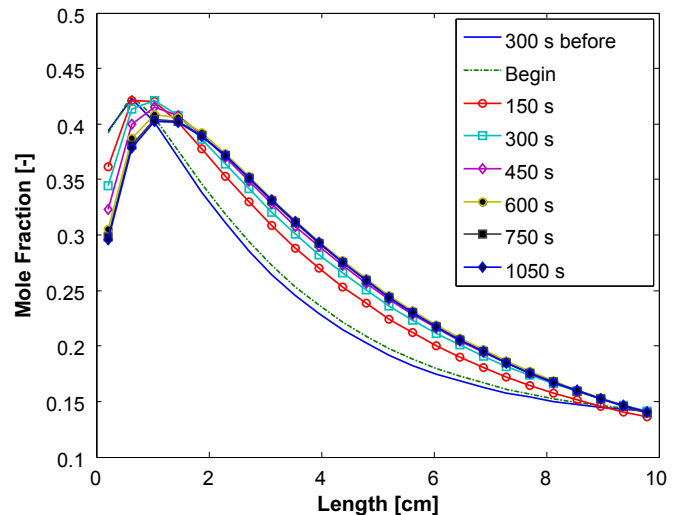


Fig. 16. Hydrogen concentration distribution during the first large dynamic of the day.

Table 3

Power output of SOFC at corresponding times during the second large dynamic of the day.

Time	Power [kW]
300 s	510.4
Begin	516.8
150 s	495.5
300 s	535.1
450 s	536.8
600 s	548.7
750 s	527.1
1050 s	495.2

From examining Table 3 and Fig. 17, it is apparent that the fuel utilization increase results in an increase of the minimum PEN temperature. It is more difficult to tell if it has an effect on the maximum PEN temperature because the power is also increasing during some of this time. The increase in PEN temperature during a fuel utilization increase can be explained by looking at the current density distribution (Fig. 18).

As the fuel utilization increased, the current density near the fuel inlet increased while the current density near the exit decreased. An increase in fuel utilization requires a decrease in fuel flow rate if the power output remains the same. While at this same power output with a decreased fuel flow rate, more current must be generated near the fuel inlet where more fuel is available (higher Nernst potential and lower concentration polarizations) because nearer the fuel exit the Nernst potential will have decreased (concentration polarizations increased). The decreased fuel flow rate can be seen by referring to Fig. 5. The increase in current density near the fuel inlet results in the minimum PEN temperature rise seen in Fig. 17.

In summary, the analysis shows that as the fuel utilization was increased the minimum PEN temperature increased as a result of increased electrochemical activity near the fuel inlet. This rise in the minimum PEN temperature, which occurred near the fuel inlet, then gave rise to an increase in the rate of SMR reactions occurring the fuel channel near the inlet.

4.2.3. Third dynamic

The third large dynamic perturbation occurred once the hydrogen storage tank became full. At this time the separated hydrogen out of the separator was re-routed to the combustor. This dynamic did not affect the intra-cell properties significantly.

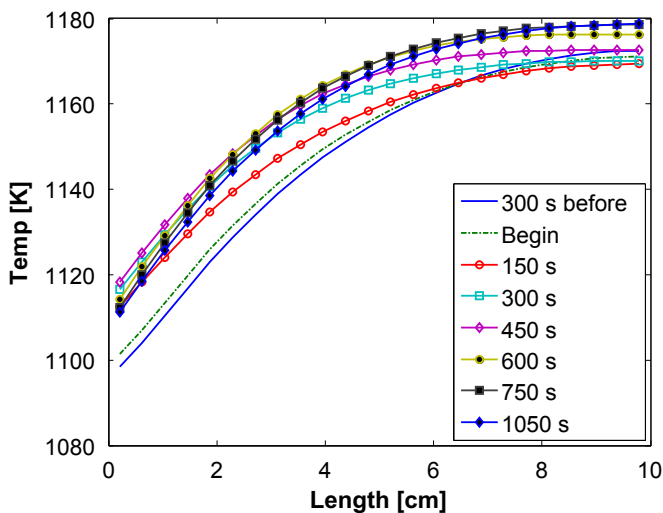


Fig. 17. PEN temperature distribution during the second large dynamic of the day.

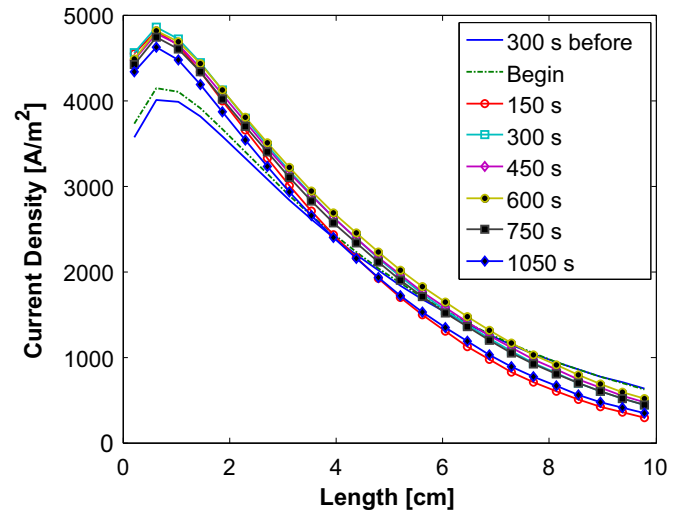


Fig. 18. Current density distribution during the second large dynamic of the day.

4.2.4. Fourth dynamic

The fourth large dynamic perturbation is the rapid decrease in power output in the early evening. This dynamic lasted only a few seconds. Most of the trends seen in this dynamic were very similar to those observed and discussed in the First Dynamic section because it is also a rapid electrical dynamic with the trends simply being inverted versus time. The major difference between these two dynamic responses is the rate at which they occur.

5. Summary and conclusions

Solid oxide fuel cells present opportunities for efficiency gains, which translate directly to CO₂ emissions reductions. These efficiency gains can be enhanced with the exploitation of synergies associated with hydrogen coproduction. As shown above, operating the fuel cell at lower utilizations, which would not make sense when only producing electricity, allows the fuel cell to operate at a higher electrochemical efficiency (i.e., polarizations are reduced), followed by collection of the excess hydrogen for later use.

While current solid oxide fuel cell systems are designed to provide base load electricity generation they have the potential to dynamically coproduce power and hydrogen. The current investigation illustrates the feasibility of following a highly dynamic building load with 3 s resolution. The dynamic system model also retains the capability to resolve information about intra-cell distributions (i.e., temperature, species concentration, current density) during these highly dynamic processes, which allows for further understanding and controls development.

Nomenclature

A	surface area: m ²
D_h	hydraulic diameter: m
\dot{E}	energy rate: kW
F	Faraday's constant: 96,485 kC kmol ⁻¹
h	convection coefficient: kW m ⁻² K ⁻¹
\dot{H}	enthalpy rate: kW
H	specific enthalpy: kJ kmol ⁻¹
I	electrical current: kA
j	current density: kA m ⁻²
LHV	lower heating value: kJ kg ⁻¹
L	length: m
J	polar moment of inertia: m ⁴
k	thermal conductivity: kW m ⁻¹ K ⁻¹

M	molar mass: kg kmol^{-1}
N	mole number:
\dot{N}	molar flow rate: kmol s^{-1}
Nu	Nusselt number: (–)
n	electron coefficient ratio: (–)
P	power or pressure: kW or kPa
\dot{Q}	heat transfer rate: kW
R	reaction rate: kmol s^{-1}
R_u	universal gas constant: $8.314 \text{ kJ kg}^{-1} \text{ K}^{-1}$
T	temperature: K
ΔT	change in temperature: K
t	time: s
U	internal energy: kJ
U_f	fuel utilization: (–)
V	voltage: V or volume: m^3
\dot{W}_{elec}	electrical power: kW
X	species mole fraction: (–)
ε	efficiency: (–)
γ	ratio of specific heats: (–)
ω	rotational speed: rad s^{-1}

References

- [1] S. Stephens-Romero, G.S. Samuelsen, *Int. J. Hydrogen Energy* 34 (2) (2009) 628–641.
- [2] H.E. Vollmar, et al., *J. Power Sources* 86 (1–2) (2000) 90–97.
- [3] E.M. Leal, J. Brouwer, *J. Fuel Cell Sci. Technol.* 3 (2) (2006) 137–143.
- [4] K. Hemmes, A. Patil, N. Woudstra, *J. Fuel Cell Sci. Technol.* 5 (4) (2008) 041010–041016.
- [5] P. Margalef, et al., *Int. J. Hydrogen Energy* 36 (16) (2011) 10044–10056.
- [6] P. Margalef, et al., *J. Power Sources* 196 (4) (2011) 2055–2060.
- [7] F. Mueller, F. Jabbari, J. Brouwer, *J. Power Sources* 187 (2) (2009) 452–460.
- [8] W. Sangtongkitcharoen, et al., *J. Power Sources* 142 (1–2) (2005) 75–80.
- [9] N. Laosiripojana, S. Assabumrungrat, S. Charojrochkul, *Appl. Catal. A Gen.* 327 (2) (2007) 180–188.
- [10] J. Meacham, in: *Mechanical and Aerospace Engineering*, University of California, Irvine, Irvine, 2005.
- [11] P. Iora, et al., *Chem. Eng. Sci.* 60 (11) (2005) 2963–2975.
- [12] F. Incropera, et al., *Fundamentals of Heat and Mass Transfer*, sixth ed., John Wiley & Sons, Hoboken, NJ, 2007.
- [13] D. McLarty, et al., *J. Power Sources* 209 (0) (2012) 195–203.
- [14] F. Mueller, et al., *J. Fuel Cell Sci. Technol.* 3 (2) (2005) 144–154.
- [15] F. Mueller, et al., *J. Fuel Cell Sci. Technol.* 4 (3) (2007) 221–230.
- [16] F. Mueller, et al., *J. Power Sources* 176 (1) (2008) 229–239.
- [17] K. Min, et al., *J. Fuel Cell Sci. Technol.* 6 (4) (2009) 041015.
- [18] R. Gaynor, et al., *J. Power Sources* 180 (1) (2008) 330–342.
- [19] R.A. Roberts, in: *Mechanical and Aerospace Engineering*, University of California, Irvine, Irvine, 2005.
- [20] R. Roberts, et al., *J. Power Sources* 161 (1) (2006) 484–491.
- [21] B. Shaffer, *Understanding Direct Internal Reformation Solid Oxide Fuel Cells with Dynamic Models and Experimentation*, University of California, Irvine, 2009.
- [22] K.J. Daun, et al., *J. Power Sources* 157 (1) (2006) 302–310.
- [23] T. Tanaka, et al., *Energy Convers. Manag.* 48 (5) (2007) 1491–1498.
- [24] B. Shaffer, J. Brouwer, *J. Fuel Cell Sci. Technol.* 9 (2) (2012).
- [25] F. Mueller, in: *Mechanical and Aerospace Engineering*, University of California, Irvine, Irvine, 2008.
- [26] J. Brouwer, et al., *J. Power Sources* 158 (1) (2006) 213–224.
- [27] F. Mueller, in: *Mechanical and Aerospace Engineering*, University of California, Irvine, Irvine, 2006.
- [28] P. Aguiar, C.S. Adjiman, N.P. Brandon, *J. Power Sources* 138 (1–2) (2004) 120–136.
- [29] S.D. Vora, in: *11th Annual SECA Workshop*, 2010. Pittsburgh, PA.
- [30] B. Shaffer, M. Hunsuck, J. Brouwer, in: *ASME Fuel Cell Science, Engineering, and Technology*, ASME, Denver, CO, 2008.